

but a clear assignment has not yet been possible because of inherent structure of the grains in the metal film.

In our experiments the coupling of light with SPs is observed in transmission rather than reflection, in contrast with previous work on SPs on reflection gratings. In those studies the coupling of light to SPs is observed as a redistribution of intensity between different diffracted orders. Even in transmission studies of wire gratings by Lochbihler¹⁵, the effect of SPs is observed through dips in zero-order transmitted light. There is an extensive literature on the infrared properties of wire grids which show a broad transmission centred at $\lambda \approx 1.2a_0$; this has been interpreted in terms of induction effects, in analogy with electric circuits^{16,17}. Our results demonstrate the strong enhancement of transmitted light due to coupling of the light with the SP of the two-dimensional array of sub-wavelength holes. Furthermore our results indicate a number of unique features that cannot be explained with existing theories. The SP modes on the metal–air interface are distinctly different from those at the metal–quartz interface. However, the spectra are identical regardless of whether the sample is illuminated from the metal or quartz side. At present we do not understand the detailed mechanism of the coupling between the SP on the front and back surfaces which results in larger than unity transmission efficiency of the holes. The thickness dependence (see Fig. 2b) suggests that the holes play an important part in mediating this coupling and that nonradiative SP modes are transferred to radiative modes by strong scattering in the holes.

In photonic bandgap arrays^{2,4}, the material is passive and translucent at all wavelengths except at the energies within the gap. In the present arrays, the material plays an active role (through the plasmons) and it is opaque at all wavelengths except those for which coupling occurs. The combination, or integration, of these two types of phenomena might lead to optical features that are very interesting from both fundamental and technological points of view. The demonstration of efficient light transmission through holes much smaller than the wavelength and beyond the inter-hole diffraction limit might, for example, inspire designs for novel near-field scanning optical microscopes⁶, or sub-wavelength photolithography. Theoretical analysis of the results would also be useful for gaining better insight into this extraordinary transmission phenomenon. Perhaps only then can we expect to grasp the full implications of these findings. □

Received 15 July; accepted 24 November 1997.

1. John, S. Localization of light. *Phys. Today* 32 (May 1991).
2. Yablonovitch, E. & Leung, K. M. Hope for photonic bandgaps. *Nature* 351, 278 (1991).
3. Dalichaouch, R., Armstrong, J. P., Schultz, S., Platzman, P. M. & McCall, S. L. Microwave localization by two-dimensional random scattering. *Nature* 354, 53–55 (1991).
4. J. D. Joannopoulos, Meade R. D. & Winn, J. N. *Photonic Crystals* (Princeton Univ. Press, Princeton, 1995).
5. Haroche, S. & Kleppner, D. Cavity quantum electrodynamics. *Phys. Today* 24 (January 1989).
6. Betzig, E. & Trautman, J. K. Near-field optics: Microscopy, spectroscopy, and surface modification beyond the diffraction limit. *Science* 257, 189–194 (1992).
7. Bethe, H. A. Theory of diffraction by small holes. *Phys. Rev.* 66, 163–182 (1944).
8. Born, M. & Wolf, E. *Principles of Optics* (Pergamon, Oxford, 1980).
9. Ritchie, R. H., Arakawa, E. T., Cowan, J. J. & Hamm, R. N. Surface-plasmon resonance effect in grating diffraction. *Phys. Rev. Lett.* 21, 1530–1533 (1968).
10. Raether, H. *Surface Plasmons* (Springer, Berlin, 1988).
11. Chen, Y. J., Koteles, E. S., Seymour, R. J., Sonek, G. J. & Ballantyne, J. M. Surface plasmons on gratings: coupling in the minigap regions. *Solid State Commun.* 46, 95–99 (1983).
12. Kitson, S. C., Barnes, W. L. & Sambles, J. R. Full photonic band gap for surface modes in the visible. *Phys. Rev. Lett.* 77, 2670–2673 (1996).
13. Watts, R. A., Harris, J. B., Hibbins, A. P., Preist, T. W. & Sambles, J. R. Optical excitations of surface plasmon polaritons on 90 and 60 bi-gratings. *J. Mod. Opt.* 43, 1351–1360 (1996).
14. Derrick, G. H., McPhedran, R. C., Maystre, D. & Neviere, M. Crossed gratings: a theory and its applications. *Appl. Phys.* 18, 39–52 (1979).
15. Lochbihler, H. Surface polaritons on gold-wire gratings. *Phys. Rev. B* 50, 4795–4801 (1994).
16. Ulrich, R. Far-infrared properties of metallic mesh and its complementary structure. *Infrared Phys.* 7, 37–55 (1967).
17. Larsen, T. A survey of the theory of wire grids. *I.R.E. Trans. Microwave Theory Techniques* 10, 191–201 (1962).

Acknowledgements. We thank S. Kishida, G. Bugmann and J. Giordmaine for their encouragement, and R. Linke, R. McDonald, M. Treacy, J. Chadi and C. Tsai for discussions. We also thank G. Lewen, G. Seidler, A. Krishnan, A. Schertel, A. Dziesiaty and H. Zimmermann for assistance.

Correspondence should be addressed to T.W.E.

Connecting atomistic and mesoscale simulations of crystal plasticity

Vasily Bulatov*, Farid F. Abraham†, Ladislav Kubin‡, Benoit Devincre‡ & Sidney Yip*

* Massachusetts Institute of Technology, Cambridge, Massachusetts 02139, USA

† IBM Research Division, Almaden Research Center, San Jose, California 95120, USA

‡ Laboratoire d'Etude des Microstructures (CNRS-ONERA), 29 Av. de la Division Leclerc, BP72, 92322 Chatillon Cedex, France

A quantitative description of plastic deformation in crystalline solids requires a knowledge of how an assembly of dislocations—the defects responsible for crystal plasticity—evolves under stress¹. In this context, molecular-dynamics simulations have been used to elucidate interatomic processes on microscopic ($\sim 10^{-10}$ m) scales², whereas ‘dislocation-dynamics’ simulations have explored the long-range elastic interactions between dislocations on mesoscopic ($\sim 10^{-6}$ m) scales³. But a quantitative connection between interatomic processes and behaviour on mesoscopic scales has hitherto been lacking. Here we show how such a connection can be made using large-scale (100 million atoms) molecular-dynamics simulations to establish the local rules for mesoscopic simulations of interacting dislocations. In our molecular-dynamics simulations, we observe directly the formation and subsequent destruction of a junction (a Lomer–Cottrell lock) between two dislocations in the plastic zone near a crack tip: the formation of such junctions is an essential process in plastic deformation, as they act as an obstacle to dislocation motion. The force required to destroy this junction is then used to formulate the critical condition for junction destruction in a dislocation-dynamics simulation, the results of which compare well with previous deformation experiments⁴.

Recent molecular-dynamics (MD) studies of dynamic crack propagation using 100 million atoms have produced massive amounts of atomic-level details on the spontaneous emission of dislocation loops from the crack tip which result in shielding, blunting and crack arrest^{2,5}. A Lennard–Jones potential is used to simulate the response of a face-centred cubic (f.c.c.) structure characterized by a low stacking-fault energy. Figure 1 shows the evolution of a ‘flower’ of dislocation loops emitted from a crack tip advancing under the action of a transverse applied strain. We shall focus on the evolution of three particular dislocation loops shown in Fig. 1, labelled 1, 2 and 3. In this sequence one sees explicitly, for the first time to our knowledge, how a dislocation junction is first formed (Fig. 1b) and then partially destroyed in a cooperative process which involves the formation of a second junction while the first junction is being unzipped (Fig. 1c). The atomic configuration of the core of the first junction, known as a Lomer–Cottrell lock, is shown in Fig. 2. Dislocation configurations of this kind are believed to be one of the principal mechanisms of strain hardening in f.c.c. metals with low stacking-fault energy.

The process of dislocation junction formation which we have identified in the MD simulation has been discussed only in schematic terms in classical textbooks^{1,6,7}, but no explicit details produced by quantitative calculations in three dimensions have (to our knowledge) been given before. The rather intricate exchange between the two junctions, apparently unforeseen and unknown, is driven by the balance between the crack-tip stress, dislocation interaction forces, the line tension forces on the mobile dislocation segments, and the constraint forces from the sessile (immobile) junctions. The destruction of Lomer–Cottrell locks has been

thought to involve rather large stresses, because the junction segment is sessile and the whole configuration is fully extended. As shown by the above sequence (Fig. 1), junction destruction is likely to proceed via ‘unzipping’, that is, motion of the dislocation node along the junction line, as was anticipated by the Friedel–Saada model¹. If this were indeed the case, then the fate of a given junction should be governed primarily by the force driving nodal

displacement, while junction extension, as determined by the stacking-fault energy, should be of secondary importance. Another implication of the observed sequence is that a quantitative physical theory of strain hardening and dynamic recovery behaviour may need to include three-body and higher-order dislocation reactions.

The present example illustrates how large-scale atomistic simulations can provide new insights into possible mechanisms of close-

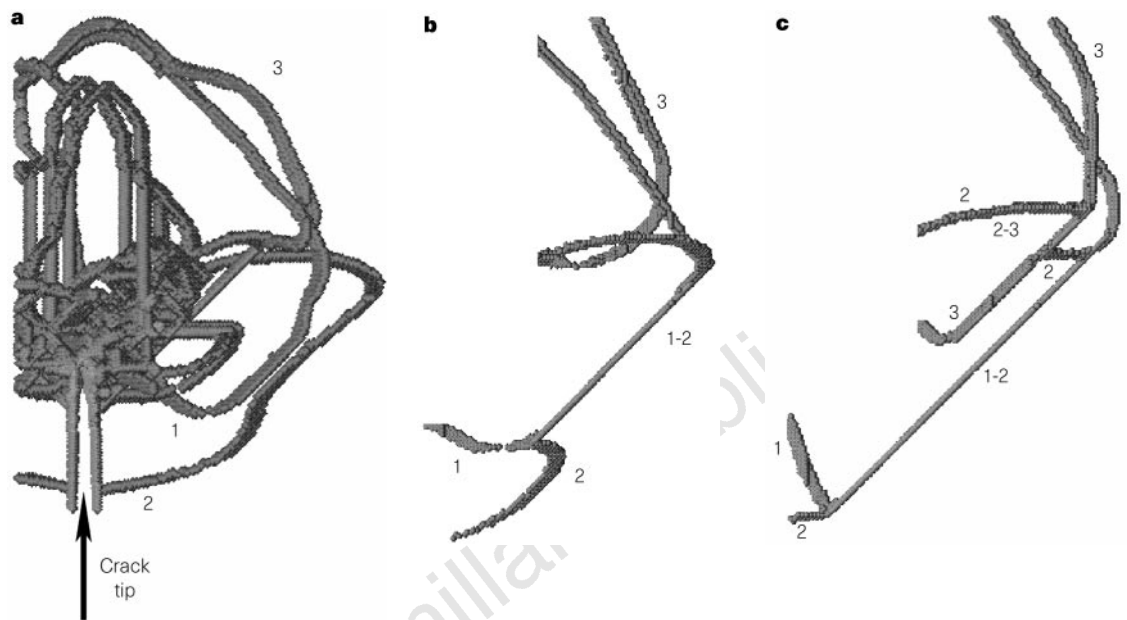


Figure 1 Evolution sequence of dislocation loops emitted spontaneously from an advancing crack tip which is suddenly arrested. In displaying the MD results, only atoms with energies exceeding the ideal bulk value by $\geq 3\%$ are shown. **a**, The expansion (spreading) of a number of dislocation loops, with loops 1 and 3 gliding in parallel (111) planes and loop 2 gliding in an intersecting (1 $\bar{1}$ 1) plane. As loops 1 and 2 approach each other, their leading segments are seen to attract each other and line up in parallel. These dislocations, on analysis, are found to be Shockley partial (imperfect) dislocations, with co-planar loops having the same Burgers vector, $a/6[11\bar{2}]$ where a is the lattice parameter, while that of loop 2 is $a/6[2\bar{1}1]$. In **b**, the leading segments of 1 and 2 have merged, forming a junction dislocation 1–2, or ‘zipper’, stretching along $[10\bar{1}]$ direction, with Burgers vector

equal to the vector sum of the Burgers vectors of the two parent dislocations: $a/6[11\bar{2}] + a/6[2\bar{1}1] = a/6[10\bar{1}]$. This reaction product, an imperfect dislocation known as a stair-rod, is sessile (immobile) because its slip plane, defined as the plane containing the line direction and Burgers vector, is not a glide plane in the f.c.c. structure. In **c**, loop 3 now glides in a plane parallel to loop 1. The elastic interaction between loop 3 and junction 1–2 is repulsive, causing loop 3 to line up along the junction. As a part of loop 3 touches the free end of the intersecting loop 2 (on the right), another junction 2–3 of the same Lomer–Cottrell type forms along the stretched segment of loop 3, while simultaneously unzipping the first junction 1–2. (Further details of fracture simulations are available at <http://www.almaden.ibm.com/st/Simulate/Fracture>)

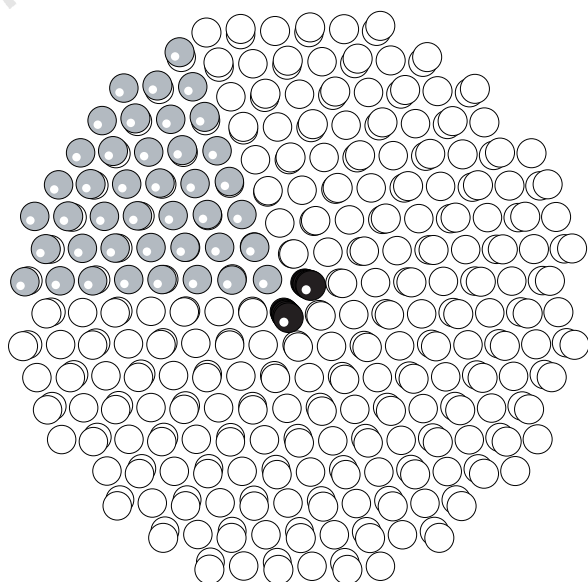


Figure 2 Atomic core structure of the junction dislocation viewed along $[10\bar{1}]$ junction line. The junction (black atoms) appears at the intersection of two stacking faults resulting from two intersecting partial dislocations, each of a mixed, 30° character with respect to the junction line direction. In terms of atomic displacement, the combination of the two partials is equivalent to carving out a triangular wedge (grey atoms) and displacing the wedge matter away from the junction by $a/6[10\bar{1}]$ and along the junction line by $a/4[10\bar{1}]$. The product dislocation is a sessile stair-rod whose core is narrow and energy is low, as indicated by the fact that only two rows of atoms (black) have energies in excess of the 3% threshold. This stair-rod is a part of the so-called Lomer–Cottrell lock⁶ which has been observed in experiments⁹.

range dislocation interactions. On the other hand, dislocation behaviour is also governed by long-range elastic interactions; a natural length scale for the collective response of dislocation microstructures is in the micrometre range. The appropriate method to treat the elastic interactions is a mesoscopic approach known as dislocation-dynamics. In this method, dislocations are represented by piecewise straight segments connecting the nodes of a regular three-dimensional mesh whose symmetries are those of the underlying crystal structure. Dislocation-dynamics simulations are currently used to examine collective dislocation behaviour on much larger scales, (typically 15 μm) for f.c.c. crystals, and longer time intervals (50 μs) than is feasible with MD. Dislocation-dynamics studies have the potential to probe the macroscopic mechanical response of single crystals controlled by the collective behaviour of dislocations at high densities: such behaviours include the formation and evolution of dislocation microstructures under stress (Fig. 3) which ultimately determine the constitutive behaviour of single crystals in various stages of plastic deformation⁸. Of particular interest is the nature of the reciprocal scaling relationship between yield stress and the length scale of dislocation patterns, postulated to date as a universal empirical 'principle of similitude'.

In dislocation-dynamics simulations, computational efficiency is achieved through a less detailed description of dislocations in which

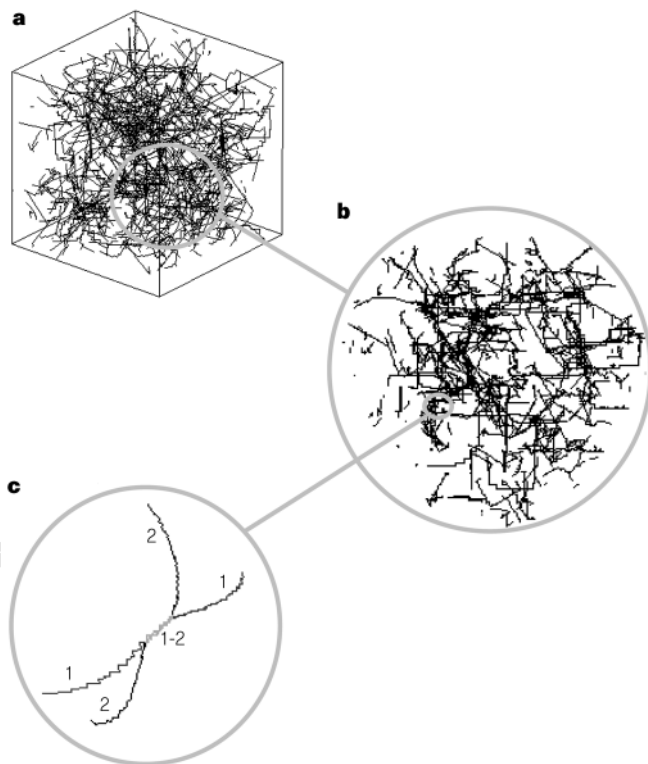


Figure 3 A composite of dislocation-dynamics simulation results. **a**, Snapshot of a dislocation-dynamics simulation where dislocations, at an initial density $2 \times 10^8 \text{ cm}^{-2}$ and placed in the simulation box at random, move in response to external and interaction stresses. **b**, A magnified interior cross-section of thickness $1 \mu\text{m}$ extracted from the simulation box of **a**; it can be seen that the dislocations are beginning to organize into a cell pattern. **c**, Further magnification showing two dislocation lines 1 and 2 tied together by a junction 1-2. The junction, formed by two perfect dislocations with Burgers vectors $a/2[101]$ and $a/2[110]$ moving under applied stress on two intersecting slip planes, (111) and $(\bar{1}11)$, respectively, is a perfect $a/2[011]$ dislocation. The parent dislocations mutually knit with each other until an equilibrium configuration is reached. The junction formation is mimicked by locking conditionally the knitted portions. (Further details of dislocation-dynamics simulations are available at <http://zig.onera.fr/lem/DisGallery>)

atomic degrees of freedom are replaced by piecewise straight lines, and a mesh spacing (a few nanometres) is used that is larger than the crystal lattice parameter. This means dislocation mobility and close-range interactions are not determined as atomic-level processes, but are specified by external parameters known as 'local rules'³. For this approach to be predictive, atomistic behaviour of dislocation cores has to be integrated into meso-scale dislocation-dynamics simulations. We therefore propose to establish a micro-to-meso connection in which the local rules are derived from the physically occurring dislocation core processes in an atomistic simulation. Figure 3c shows the formation, in a meso-scale simulation, of an attractive junction under conditions close to the MD simulation described above. The behaviour of this mesoscopic junction needs to be matched to the behaviour of its atomistic analogue, such as the one shown in Fig. 1b.

Evolution of the junction, zipping further or unzipping, will depend on the forces acting on the two mobile segments connected to each node at the junction's end (nodal segments). It is the junction strength that governs the strain-hardening properties of f.c.c. crystals (so-called stage II hardening). We now analyse the junction strength in terms of the minimum force required to drive the unzipping process. In general, the force F acting to separate the junction is the Peach–Koehler force, τb , where τ is the stress on the mobile nodal segment and b is the magnitude of its Burgers vector, times the effective arm-length of the segment l . The critical condition for unzipping is that F should be equal to the energy spent on separating a unit length of the junction and moving the resulting partials apart by a distance l . This energy is the sum of core W_c and elastic W_{el} contributions. Practically, for mesoscopic simulations, junction strength is treated through an effective junction stress $\tau_j = (W_c + W_{el})/bl$, which is then combined with the local stress τ acting on every segment connected to a junction node. Although τ_j is not a material parameter itself, as it depends on the length of the unzipping arm, the local rule for mobility of the nodal segments is nevertheless fully specified, once W_c and W_{el} are known. Whereas W_{el} can be calculated from elasticity theory, the core contribution W_c can only be determined atomistically.

We have carried out an explicit atomistic calculation to obtain the core contribution W_c . To avoid the complications of dealing with non-uniform stress distributions near a crack tip, we analyse the energetics of junction unzipping in the same crystal without the crack and under zero stress. The energy cost of junction unzipping was obtained by comparing the energy of a sufficiently large cylindrical slab (559.6 \AA in diameter) centred around lock 1-2 (Fig. 1b) with the energy of the same slab for a configuration where partials 1 and 2 are lined up parallel at a distance d , similar to that shown in Fig. 1a. Presenting our result in a form scaled to the length l of the mobile segment, the effective junction stress is given by the above equation with $W_c(b) = -0.0542 \text{ eV } \text{\AA}^{-1}$ and $W_{el}(lb) = 0.106 \ln(lb) \text{ eV } \text{\AA}^{-1}$, $b = 1.65 \text{ \AA}$. These numerical values were obtained for Lennard–Jones potential with well depth $\epsilon = 0.15 \text{ eV}$ and length parameter $\sigma = 2.556 \text{ \AA}$, nominally representing Cu. For the arm length of $0.5 \mu\text{m}$, the effective junction stress is 15.5 MPa, which compares very well with the junction strength parameter previously obtained by fitting mesoscopic simulation data to deformation experiments⁴.

The overlap of atomistic and continuum length scales, demonstrated in this work for the case of dislocation junctions, points to the feasibility of a critical connection between two different modelling methodologies. It should lead to significantly improved understanding of dislocation behaviour which up to now has been investigated mostly within the framework of linear elasticity. As well as the properties of dislocation locks and junctions, a host of other essential mechanisms could be elucidated, including the cross-slip properties of screw dislocations, the dynamics of the formation and motion of kink pairs, and the annihilation properties of closely spaced edge-dislocation dipoles. \square

Received 1 October; accepted 30 December 1997.

1. Friedel, J. *Dislocations* (Pergamon, Oxford, 1964).
2. Abraham, F. F. *et al.* Instability dynamics in three-dimensional fracture: an atomistic approach. *J. Mech. Phys. Solids* **45**, 1461–1471 (1997).
3. Devincere, B. & Kubin, L. P. Mesoscopic simulations of dislocations and plasticity *Mater. Sci. Eng. A234–236*, 8–14 (1997).
4. Devincere, B. & Kubin, L. Simulations of forest interactions and strain hardening in FCC crystals. *Modelling Simul. Mater. Sci. Eng.* **2**, 559–570 (1994).
5. Abraham, F. F. On the transition from brittle to plastic failure in breaking a nanocrystal under tension. *Europhys. Lett.* **38**, 103–106 (1997).
6. Hirth, J. P. & Lothe, J. *Theory of Dislocations* 2nd edn 792–806 (Wiley, New York, 1982).
7. Nabarro, F. R. N. *Theory of Crystal Dislocations* (Oxford Univ. Press, London, 1967).
8. Prinz, F. & Argon, A. S. Dislocation cell formation during plastic deformation of copper single crystals. *Phys. Status Solidi A* **57**, 741–753 (1980).
9. Korner, A. & Karnthaler, H. P. Weak-beam studies of composite dislocations gliding on (001) planes in Si. *Phil. Mag.* **44**, 275–284 (1981).

Acknowledgements. This work originated at a collaborative workshop on materials modelling held at the Institute for Theoretical Physics, UCSB, during March 1997. F.F.A. acknowledges the use of the Cornell Theory Center, which receives funding from the NSF and New York State; B.D. and L.K. acknowledge the support of CNRS through the GDR programme on mesoscopic simulations and modelling in metallurgy; V.B. and S.Y. acknowledge support from LLNL; and V.B. acknowledges support from the Alcoa Foundation.

Correspondence and requests for materials should be addressed to V.B. (e-mail: vasily@mit.edu).

Impact energy measurement in time-of-flight mass spectrometry with cryogenic microcalorimeters

G. C. Hilton*, John M. Martinis*, D. A. Wollman*, K. D. Irwin*, L. L. Dulcie*, Daniel Gerber†, Patrick M. Gillevet‡ & Damian Twerenbold†

* National Institute of Standards and Technology, Boulder, Colorado 80303, USA

† Institut de Physique de l'Université Rue A.-L. Breguet 1, CH-2000 Neuchâtel, Switzerland, and GenSpec SA, case postale 120, CH-2017 Boudry, Switzerland

‡ Institute of Bioscience, Bioinformatics, and Biotechnology, George Mason University, Manassas, Virginia 22210, USA

Time-of-flight mass spectrometry—most notably matrix-assisted laser-desorption-ionization time-of-flight (MALDI-TOF) spectrometry¹—is an important class of techniques for the study of proteins and other biomolecules². Although these techniques provide excellent performance for masses up to about 20,000 daltons, there has been limited success in achieving good mass resolution at higher masses. This is because the sensitivity of the microchannel plate (MCP) detectors used in most systems decreases rapidly with increasing particle mass, limiting the utility of MCP detectors for very large masses. It has recently been proposed that cryogenic particle detectors may provide a solution to these difficulties³. Cryogenic detectors measure the thermal energy deposited by the particle impact, and thus have a sensitivity that is largely independent of particle mass. Recent experiments^{4–6} have demonstrated the sensitivity of cryogenic particle detectors to single biomolecules, a quantum efficiency several orders of magnitude larger than the MCP detectors, and sensitivity to masses as large as 750,000 daltons. Here we present results demonstrating an order of magnitude better energy resolution than previous measurements, allowing direct determination of particle charge state during acceleration⁷. Although application of these detectors to practical mass spectrometry will require further development of the detectors and cryogenics, these detectors can be used to elucidate the performance-limiting processes that occur in such systems.

In the past several years, significant progress has been made in developing high-performance cryogenic detectors for applications such as infrared bolometry and X-ray, visible and ultraviolet spectroscopy. These detectors fall into two classes: non-equilibrium

devices such as superconducting tunnel junctions (STJs)^{8,9}, and equilibrium devices such as microcalorimeters^{10–13}. The previous experiments^{4,5} with cryogenic particle detectors for mass spectrometry used STJs, which fail to record the total impact energy because they are insensitive to the fraction of impact energy deposited as phonons with energy less than the superconducting gap. In this experiment we used a normal-insulator-superconductor microcalorimeter fabricated on a thin Si₃N₄ membrane, which detects all of the thermal energy deposited by a particle impact. Although the speed and energy resolution performance of our detector is sufficient for this preliminary experiment, experience with other applications indicate that significantly better performance should be possible in the future. It is important to note that the collection area of the cryogenic detectors studied is more than 10⁴ times smaller than typical MCP detectors. Although this size can be improved in the future, the overall sensitivity (the product of quantum efficiency and collection area) of this detector is significantly less than MCP detectors except at extremely large (>100,000 daltons) masses⁶.

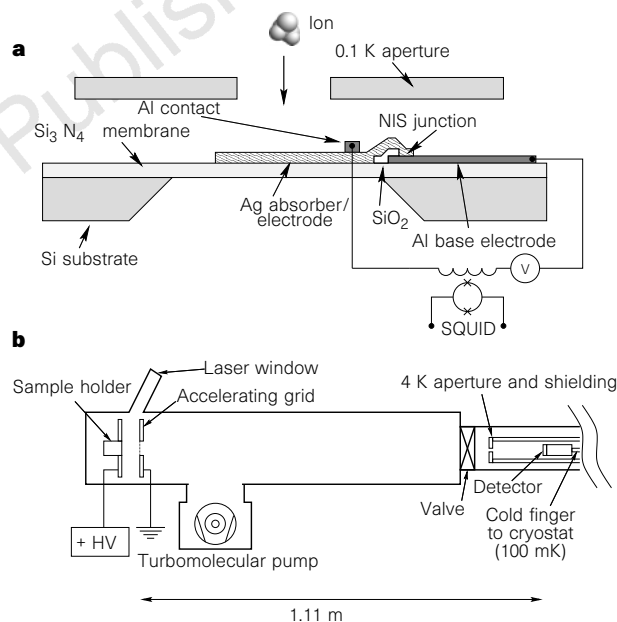


Figure 1 Details of experimental apparatus. **a**, Cross-section of the normal-insulator-superconductor (NIS) microcalorimeter. An accelerated molecule flies through a 200-µm-diameter 0.1 K aperture and strikes the absorber (a 100-nm-thick Ag film measuring 200 µm × 200 µm deposited on a 0.5-µm-thick Si₃N₄ membrane), raising the absorber temperature. This temperature rise is detected as a current pulse produced by a voltage-biased NIS junction, which consists of a thinly oxidized Al electrode in contact with the absorber. The junction current is measured by a SQUID preamplifier. Contacts to the detector are provided by superconducting Al leads which carry electrical current but do not conduct heat. **b**, Schematic view of our MALDI-TOF spectrometer indicating detector placement and infrared shielding. The infrared shielding consists of a 1-mm-diameter aperture cooled to 4 K and placed 10 cm away from the detector. Ions are created when laser light pulses (337 nm, 3 ns, maximum power 100 µJ) strike the probe plate. Ions are accelerated by an electric field between the probe plate and the grounded fine-mesh accelerating grid. Vacuum in the spectrometer is provided by a 110 l s⁻¹ turbomolecular pump, attaining a base pressure in the 100-mm-diameter flight tube of 2 × 10⁻⁵ Pa (1.5 × 10⁻⁷ torr). Two proteins were studied, lysozyme (mass 14,300 daltons) and bovine serum albumin (BSA, mass 66,430 daltons). In both cases proteins solutions were prepared by combining 1 mg of protein with 1 ml of a 0.1% trifluoroacetic acid H₂O solution. The matrix solution consisted of 100 mg sinapinic acid (mass 224 daltons) dissolved in 6 ml of ethanol and 4 ml H₂O. Probes were prepared by mixing 40 µl each of the probe and matrix solutions and allowing the mixture to dry in air on the probe plate.